Interannual Spatiotemporal Variations of Land Surface Temperature in China From 2003 to 2018

Yanru Yu, Si-Bo Duan, Zhao-Liang Li, Sheng Chang, Zefeng Xing, Pei Leng, and Maofang Gao

***Abstract*—Land surface temperature (LST) is a comprehensive embodiment of surface energy balance and land surface processes. The spatial and temporal variation of LST is of great significance for studying surface characteristics and climate change. In this study, the spatiotemporal variations of LST in China from 2003 to 2018 is examined by using the continuous and derivable annual temperature cycle model. The trends of the annual mean and annual amplitude of LST is detected using the Mann–Kendall test and Theil–Sen estimator. In addition, we have further revealed the correlation between normalized difference vegetation index (NDVI) and LST in different land cover types. The results show that the annual mean LST presents a spatial distribution pattern of high values in the southern regions and low values in the northern regions and that the factors of altitude and land cover type also affect the LST's spatial distribution. The annual amplitude of the LST presents a spatial distribution pattern of high values in the northern regions and low values in the southern regions. In the majority of instances, the phase of LST in China was positioned between the 175th and 205th day of each year. Both the annual mean and annual amplitude of the LST have a mean increasing trend in China with a rate of 0.02 K/year, and the areas with large significant changes accounted for 8.6% out of the total area, with a mean rate of approximately 0.05 K/year, in this period. Significant changes in the annual mean LST were correlated with the change in vegetation coverage and the impact of land cover types on the interannual variations of LST is also determined in this study. While the increase in vegetation coverage in barren land exhibits a clearly recognizable upward trend in the annual mean LST, the improved vegetation coverage in the grassland region presents a downward trend in annual mean LST.**

Manuscript received October 16, 2020; revised December 9, 2020; accepted December 28, 2020. Date of publication January 1, 2021; date of current version January 21, 2021. This work was supported in part by the National Key R&D Program of China under Grant 2018YFB0504800 and Grant 2018YFB0504804, in part by the National Natural Science Foundation of China under Grant 41871275, and in part by the Fundamental Research Funds for Central Non-Profit Scientific Institution under Grant 1610132020044. *(Corresponding authors: Si-Bo Duan; Sheng Chang.)*

Yanru Yu, Si-Bo Duan, Zefeng Xing, Pei Leng, and Maofang Gao are with the Key Laboratory of Agricultural Remote Sensing, Ministry of Agriculture and Rural Affairs/Institute of Agricultural Resources and Regional Planning, Chinese Academy of Agricultural Sciences, Beijing 100081, China (e-mail: 82101181155@caas.cn; duansibo@caas.cn; xingzf19900720@163.com; lengpei@caas.cn; gaomaofang@caas.cn).

Zhao-Liang Li is with the Key Laboratory of Agricultural Remote Sensing, Ministry of Agriculture and Rural Affairs /Institute of Agricultural Resources and Regional Planning, Chinese Academy of Agricultural Sciences, Beijing 100081, China, and also with the State Key Laboratory of Resources and Environment Information System, Institute of Geographic Sciences and Natural Resources Research, Chinese Academy of Sciences, Beijing 100101, China (e-mail: lizhaoliang@caas.cn).

Sheng Chang is with the State Key Laboratory of Remote Sensing Science, Aerospace Information Research Institute, Chinese Academy of Sciences, Beijing 100101, China (e-mail: changsheng@aircas.ac.cn).

Digital Object Identifier 10.1109/JSTARS.2020.3048823

***Index Terms*—Land surface temperature, Moderate Resolution Imaging Spectroradiometer (MODIS), spatiotemporal variation, trend analysis.**

I. Introduction

REGIONAL and global climate change has increasingly attracted the attention of researchers over the past century. The rise in temperature is a topic of major concern in the context of climate change, and it shares a similar temporal and spatial heterogeneity with climate change [1]. Therefore, the study of spatiotemporal variation in temperature is particularly important. Many previous studies have focused on the temporal and spatial changes of surface air temperature. Ji *et al*. [2] analyzed the evolution of land surface air temperature trends by using data from the Climatic Research Unit. Kagawa-Viviani and Giambelluca [3] characterized the spatiotemporal patterns of surface air temperature in the Hawaiian Islands. In addition, research exploring the driving factors of surface air temperature trends [4] and observing the differences between air temperature and skin temperature are also significant in this respect [5].

There are many studies that reveal the surface energy balance based on air temperature. Although surface air temperature and land surface temperature (LST) are locally correlated, there are obvious differences between surface air temperature and LST in terms of magnitude [6]. Compared to air temperature, LST has a faster response to the changes in regional energy balance, and LST reflects the spatial and temporal changes of surface energy and surface characteristics instantaneously. Moreover, air temperature data are mostly ground station data or reanalysis data. Thus, it cannot be spatiotemporally analyzed in continuous space as it either does not meet the requirements for conducting the analysis or is too coarse to guarantee accuracy. Remote sensing satellites provide a useful and powerful database for evaluating the dynamics of LST because of their wide coverage and quick imaging technology. Therefore, research on the spatiotemporal changes of LST derived from satellites is more representative of the changes in surface energy and surface characteristics.

The availability of long-term LST data derived from the Moderate Resolution Imaging Spectroradiometer (MODIS) has motivated many scientists to study interannual variations of LST [7]–[9]. MODIS LST products have also been used for assessing the urban heat islands effect [10], [11] and drought monitoring [12].

Satellite-derived LST has recently been used to explore annual temperature cycle (ATC) variations at a regional and global scale because of its large spatial coverage and high revisit frequency. Bechtel [13] initially proposed the ATC model to obtain LST parameters and was later used by him to characterize the urban thermal landscapes [14]. The reason why the ATC model is widely used is that the LST parameters obtained from the ATC model can fully express the changes in surface thermal behavior and reflect the feedback effect of surface thermal behavior on climate change. Zhao *et al*. [15] applied the ATC model over the mountainous region impacted by the 2008 Wenchuan earthquake and displayed spatiotemporal variability in the LST of this region. Quan *et al*. [16] proposed a decomposition of the ATC model to extract the trend, seasonal, and noise components of LST in continuous space for detecting the seasonal variations of the LST from 2000 to 2012. They further investigated the trends and seasonal patterns of surface urban heat islands. Sismanidis *et al*. [17] provided a spatiotemporal dynamic map of the LST of mainland Europe and a data set to support climate classification at a finer spatial resolution.

As LST is a dynamic parameter, its variation is affected by many factors including precipitation [18], elevation [19], air temperature [20], land cover types [21], and vegetation index (NDVI) [22]. Among these, NDVI and land cover type have been shown to be closely correlated to the variation of LST [23]–[25]. Deng *et al*. [26] analyzed the relationship between LST and NDVI in a typical karst area, and the results showed that the spatial distributions of NDVI and LST exhibited opposite patterns in the study area. Peng *et al*. [27] investigated the effects of afforestation on LST using the MODIS LST data and found that afforestation has a cooling effect on daytime LST and a warming effect on nighttime LST. In dry regions, afforestation leads to net warming because daytime cooling is offset by nighttime warming. Generally, while high-latitude and high-altitude areas where vegetation growth is restricted by energy show a positive correlation between NDVI and LST, areas where vegetation growth is restricted by water show a negative correlation between NDVI and LST [28]. Furthermore, the magnitude of the correlations between NDVI and LST is related to the land cover type [29].

The spatiotemporal variation of LST is important for detecting changes in land surface characteristics and understanding climate change. China is the third largest country in the world with a variety of climate types, diverse land cover types, and a large degree of topographical relief. This makes it imperative to assess the variations of LST across the country for climate applications and environmental planning. In this study, we analyzed the spatiotemporal patterns of LST in China with the MODIS daily LST products from 2003 to 2018, using an ATC model developed by Xing *et al*. [30]. The ATC model is a continuous and derivable model, which is suitable for the study of variation in LST in continuous temporal and spatial space. The rest of the article is structured as follows. Section II reports the data used in this study. Section III presents the ATC model and the analysis methods. Section IV presents and discusses the results. Finally, Section V concludes.

II. Data

MODIS is mounted on the Terra and Aqua satellites and obtains data via the high frequency of two observations per day. In this study, MODIS land products were selected for the period from 2003 to 2018.

The 1-km LST product (MYD11A1) was used to calculate the daily mean LST, with the maximum–minimum method, to investigate the spatiotemporal variability of LST across China [31]. We selected observations from the Aqua satellite instead of the Terra satellite because the overpass time of Aqua satellite is 1:30 P.M./A.M. According to the diurnal temperature cycle (DTC) of LST [32], the observations at 1:30 P.M./A.M. give an approximate value of daily maximum and minimum temperature. The LST observations were controlled by the quality assurance (QA) file to ensure that the average LST error was less than 2.0 K. In order to ensure a higher precision fitting of the ATC model, the pixels with less than 10 days of cloud-free data within a year were not considered in the analysis.

The 1-km 16-day NDVI product (MOD13A2) was applied to detect the variation in vegetation coverage among the different land cover types over the study period. In order to eliminate the interference of clouds on the NDVI products, quality assurance data were used to obtain the NDVI data without the influence of clouds and to derive the annual maximum NDVI value for each year.

In addition, the land cover product (MCD12Q1) was used in this study. It contains the International Geosphere-Biosphere Programme (IGBP) global vegetation classification scheme, which identifies 17 classes. In this study, the IGBP scheme was grouped into nine classes [33], and the land cover type of water was not considered. The classes of evergreen needleleaf forest, evergreen broadleaf forest, deciduous needleleaf forest, deciduous broadleaf forest, and mixed forest were categorized as forest regions in IGBP. Closed shrubland and open shrubland regions were classified as shrubland regions. Woody savannas and savannas were grouped as woodland regions, and cropland and cropland/natural vegetation mosaic were categorized as cropland regions. The MCD12Q1 data were spatially aggregated to match the spatial resolution of LST data. Fig. 1(a) shows the spatial distributions of the nine land cover types in China in 2018. These MODIS products can be downloaded via NASA Earth science Data.[1]

Climate division data were obtained from the China Meteorological Administration. The classification of climate regions is based on differences in the water and heat properties, and each climate region has its specific surface thermal characteristics. LST is an important indicator to characterize the thermal properties of land surface. Therefore, we analyzed the interannual variation of LST combined with the climate regions. Fig. 1(b) shows the specific climate regions in China, and the background map is derived from the digital elevation model (DEM) data.

III. Methods

A. Annual Temperature Cycle Model

Bechtel [13] proposed an ATC model with three parameters (referred as ACP3) to simulate the annual variation of LST. This model consists of a constant term and a sine function with the spring equinox as the reference day to describe the changes in

[1] [Online]. Available: https://search.earthdata.nasa.gov.

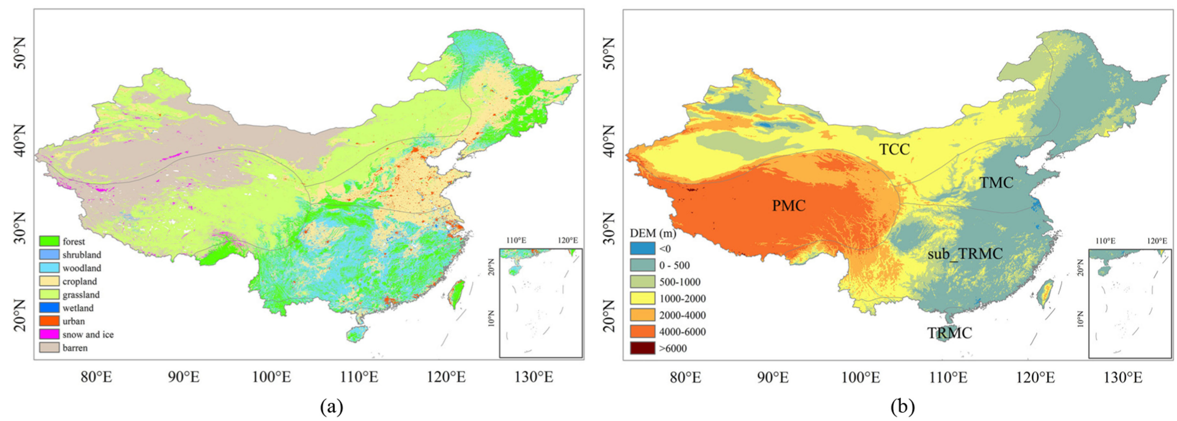

Fig. 1. (a) Land cover types of China in 2018 derived from MODIS, and the 9 classes derived from 17 classes of IGBP. (b) Geographical locations of the climate regions of temperate continental climate (TCC), temperate monsoon climate (TMC), plateau mountain climate (PMC), subtropical monsoon climate (sub_TRMC), and tropical monsoon climate (TRMC).

LST over the year. Taking into account that the annual cycle of irradiation in the tropics is characterized by two annual maxima instead of one, Bechtel *et al.* [34], [35] further developed another ATC model with a second harmonic function (referred as ACP5) to replace the ACP3 in the tropics. Because the study area is mainly distributed in midlatitudes, the ACP3 model has more advantages than the ACP5 model in terms of fitting accuracy.

In this study, to characterize the date when the LST reaches its maximum value of the year, a cosine function instead of a sine function is used in the ACP3 model. This model is formulated as

$$\mathrm{LST(t)} = a + b\cos\left[\frac{2\pi}{\omega}(t-c)\right] \tag{1}$$

where LST is the average of daytime and nighttime cloud-free LST; t is the day of year; a is the annual mean LST; b is the annual amplitude of LST; c is the phase, which represents the day when LST reaches its maximum value of the year; and ω is the annual cycle, which is 365 days in a normal year and 366 days in a leap year. The specific physical meaning of the model parameters is shown in Fig. 2.

To better characterize the dynamics of multiyear annual temperature cycles, Xing *et al.* [30] developed a continuous and derivable ATC model for multiyear fitting of LST, based on the model mentioned above. This continuous and derivable ATC model is formulated as

$$\begin{cases} \mathrm{LST}^{i}(\mathrm{t}) = a^{i} + b^{i}\cos[\frac{2\pi}{\omega}(t-c^{i})] \\ \mathrm{LST}^{i+1}(\mathrm{t}) = a^{i+1} + b^{i+1}\cos[\frac{2\pi}{\omega}(t-c^{i+1})] \end{cases} \tag{2}$$

with

$$\begin{cases} a^{i+1} = a^{i} + b^{i}\cos[\frac{2\pi}{\omega}(365i + k_{i+1} + 0.5 - c^{i})] \\ -b^{i+1}\cos[\frac{2\pi}{\omega}(365i + k_{i+1} + 0.5 - c^{i+1})] \\ b^{i+1} = \frac{b^{i}\sin[\frac{2\pi}{\omega}(365i+k_{i+1}+0.5-c^{i})]}{\sin[\frac{2\pi}{\omega}(365i+k_{i+1}+0.5-c^{i+1})]} \end{cases} \tag{3}$$

where i is the year number of the years, t represents the day of the year, $t \in [365(i-1) + k_i + 1, 365i + k_{i+1}]$, and k_i is the number of leap years before year i.

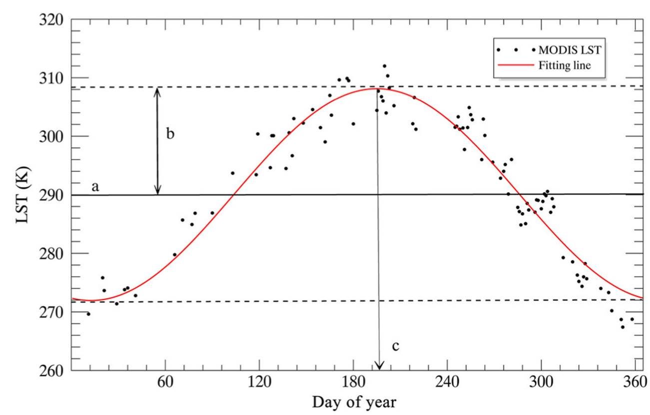

Fig. 2. Description of parameters in the ATC model: a is the annual mean LST, b is the annual amplitude of LST, and c is the phase, which represents the day when LST reaches its maximum value of the year.

In this study, we used the continuous and derivable ATC model to simulate the interannual spatiotemporal variations of LST. The annual mean LST, annual amplitude of LST, and annual phase of LST, from 2003 to 2018, were derived from the continuous and derivable ATC model.

B. Trend Analysis

The trend of annual mean LST and annual amplitude of LST from 2003 to 2018 was detected by the Mann–Kendall test [36], which is a nonparametric test used for identifying trends in a time series data. This test is often used for conducting a trend analysis of the factors of climate change. Its advantage is that the samples do not need to follow a certain distribution and that it is minimally affected by the missing values. The change trends of the annual mean LST and annual amplitude of LST during the study period were calculated by the Theil–Sen estimator, also known as Sen's slope estimator [37]. A detailed description of the Mann–Kendall test and Theil–Sen estimator can be found in previous studies [38].

1) Mann–Kendall Test: The Mann–Kendall test statistic S is defined as

$$S = \sum_{i=1}^{n-1} \sum_{j=i+1}^{n} \mathrm{sgn}(x_j - x_i) \tag{4}$$

where n is the number of data points; x_i and x_j are the data values in time series i and j ($j > i$), respectively; and sgn is the sign function. The term "sgn" is defined as

$$\mathrm{sgn}(x_j - x_i) = \begin{cases} +1 & x_j - x_i > 0 \\ 0 & x_j - x_i = 0 \\ -1 & x_j - x_i < 0 \end{cases}. \tag{5}$$

The variance is computed as

$$\mathrm{Var}(S) = \frac{n(n-1)(2n+5) - \sum_{i=1}^{m} t_i(t_i - 1)(2t_i + 5)}{18} \tag{6}$$

where m is the number of tied groups and t_i is the number of data points in the ith tied group. When $n > 10$, the standard normal test statistic Z_s is expressed as

$$Z_s = \begin{cases} \frac{S-1}{\sqrt{\mathrm{Var}(S)}} & S > 0 \\ 0 & S = 0 \\ \frac{S+1}{\sqrt{\mathrm{Var}(S)}} & S < 0 \end{cases}. \tag{7}$$

The sign of Z_s indicates the data trend direction. A positive value of Z_s indicates an ascending (increasing) trend, and the negative value shows a descending (decreasing) trend. A significant level α was specified before the trend test. When $|Z_s| > Z_{1-\alpha/2}$, the null hypothesis is rejected. This indicates that the data show a significant trend in the detected time series. $Z_{1-\alpha/2}$ is obtained from the standard normal distribution table. In this study, the Mann–Kendall test was run at $\alpha = 0.05$ significance level. When $|Z_s| > 1.96$, it indicates that the data passed the test with a 95% confidence interval.

2) Theil–Sen Estimator: Sen [37] developed a nonparametric procedure for estimating the slope of a trend in the sample of N pairs of data. This procedure is formulated as

$$Q_k = \frac{x_j - x_i}{j - i}, k = 1, \ldots, N \tag{8}$$

where x_j and x_i are the data values at times j and i ($j > i$), respectively. The N values of Q_k are ranked from the smallest to the largest, and the median of slope or the Theil–Sen estimator is formulated as

$$Q_{med} = \begin{cases} Q_{[(N+1)/2]}, N \in \text{odd} \\ \frac{Q_{[N/2]} + Q_{[(N+2)/2]}}{2}, N \in \text{even} \end{cases}. \tag{9}$$

The sign of Q_{med} reflects the data trend and its value indicates the steepness of the trend.

3) Correlation Analysis: The Pearson correlation coefficient is widely used to measure the degree of correlation between two variables. If two random variables X and Y are composed of N independent individuals of (X_1, X_2, …, X_N) and (Y_1, Y_2, …, Y_N), respectively, then the Pearson correlation coefficient (r) between X and Y is defined as

$$r = \frac{\sum_{i=1}^{N} (X_i - \overline{X})(Y_i - \overline{Y})}{\sqrt{\sum_{i=1}^{N} (X_i - \overline{X})^2} \sqrt{\sum_{i=1}^{N} (Y_i - \overline{Y})^2}} \tag{10}$$

with

$$\begin{cases} \overline{X} = \frac{1}{N} \sum_{i=1}^{N} X_i \\ \overline{Y} = \frac{1}{N} \sum_{i=1}^{N} Y_i \end{cases}. \tag{11}$$

In this study, the Pearson correlation coefficient was used to analyze the correlation between the annual mean LST and annual maximum value of NDVI. It was also used to further reveal the impact of land cover types on the interannual variations of LST.

IV. Results and Discussion

A. Spatial Pattern of Annual Mean LST and Annual Amplitude of LST

Fig. 3 displays the spatial distribution of annual mean LST in China, from 2003 to 2018, by considering the data obtained at three-year intervals within the study period. The blank areas in Fig. 3 are pixels with missing data due to the impact of cloudy and rainy weather. As the spatial pattern of the annual mean LST in China is very similar from year to year, only six years of data were selected for presenting the results of this study. The annual mean LST varies from 260 to 310 K across China. As the latitude increases, the solar radiation energy received by the ground decreases. This results in the overall distribution pattern of annual mean LST with high values in the southern regions and low values in the northern regions. However, there are also some areas that do not follow this pattern. The Qinghai–Tibet Plateau is located in the middle and low latitudes. It has a relatively lower annual mean LST because the Qinghai–Tibet Plateau is the highest altitude area in China with an average altitude of more than 4000 m. As the plateau is situated at a high altitude, the air near the surface is thin, which leads to poor heat preservation on the ground and further results in a lower annual mean LST as compared to other areas [39]. Another area that shows abnormal properties is Tarim Basin, a high latitude area located in northwestern China. The annual mean LST in this region is higher than in the eastern part with the similar latitude. Taking into consideration the geographical characteristics of the area, it is observed that the low elevation increases the thermal insulation inside the basin [40]. Regarding the land cover type factor, the largest desert in China is located in this basin, which absorbs solar radiation. At the same time, the Tianshan Mountains, located to the north of the basin, block cold air from the north, further increasing the temperature in this area.

In terms of different climatic regions, the tropical monsoon climate (TRMC) region has the highest annual mean LST, with the annual mean LST varying between 295 and 305 K. The sub_TRMC region follows the TRMC region in this respect, and the annual mean LST in this region typically ranges from 290 to 300 K. The TMC region is the transitional region between the temperate and subtropical climate regions in China. The annual mean LST in this region is approximately 283 K, but it shows

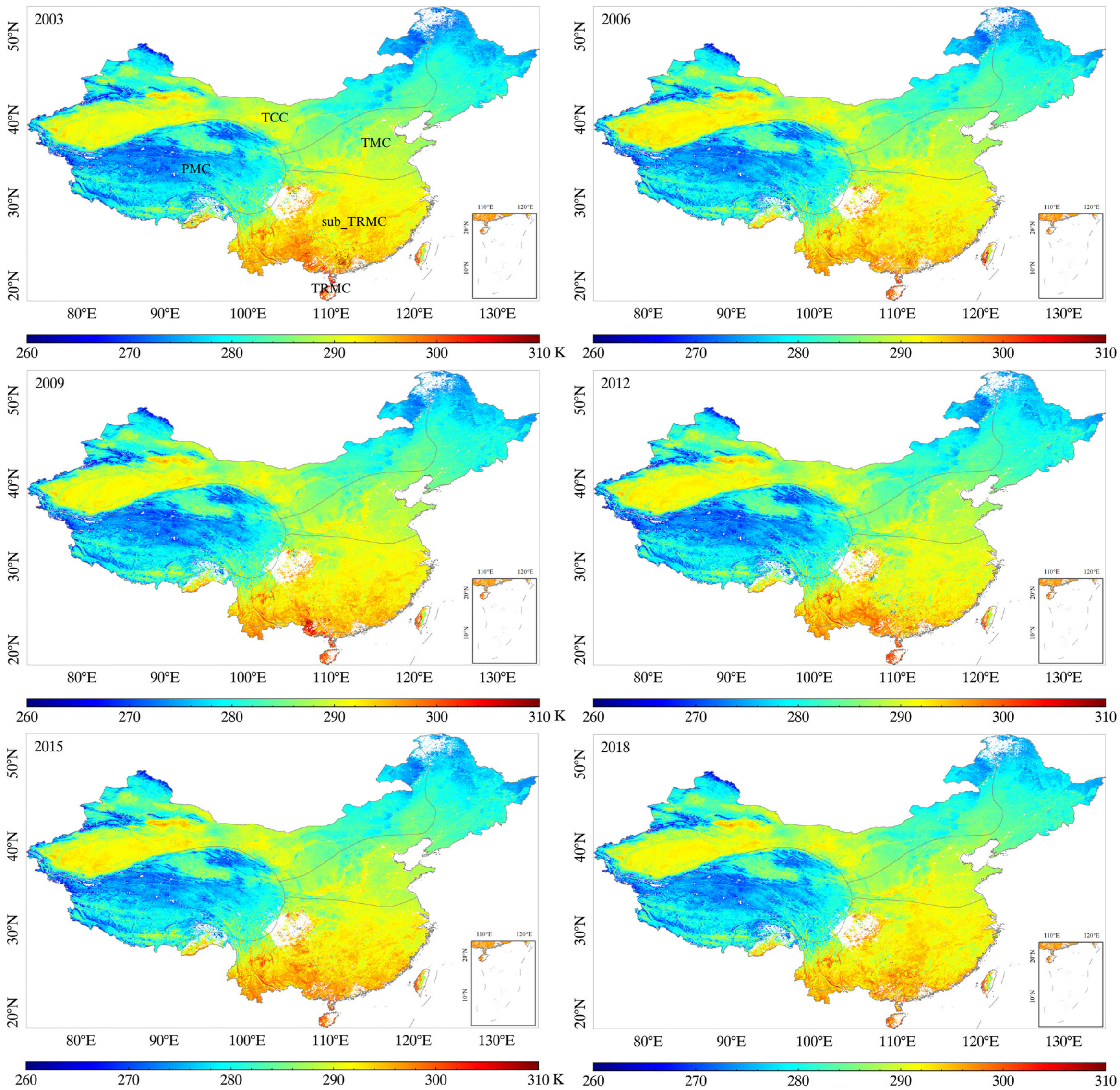

Fig. 3. Spatial distribution of annual mean LST in 2003, 2006, 2009, 2012, 2015, and 2018. The blank areas in the maps are areas with missing satellite data due to cloud contamination. The climate regions of TCC (temperate continental climate), TMC (temperate monsoon climate), PMC (plateau mountain climate), sub_TRMC (subtropical monsoon climate), and TRMC (tropical monsoon climate) are also shown.

great spatial variation. The annual mean LST in the northern part of TMC region is as low as 270 K, but in the southern part of TMC region, it can reach 290 K. Due to high altitude, the annual mean LST in the PMC region has the lowest value, approximately 277 K.

To further show the changes of LST from 2003 to 2018, we analyzed the annual mean LST difference between 2003 and 2018. Positive (negative) value indicates the warming (cooling) of LST. Fig. 4(a) and b shows the spatial distribution of LST difference and the variation in different latitude, respectively. There is more warming in the north China and less in the south China, resulting in the largest warming effect in the northeastern (above 40 °N), moderate warming effect in the mid latitudes (35–40 °N). The LST difference is closed to 0 K between 30 and 35 °N, while below 30 °N is mainly cooling, and the strongest cooling effect is distributed between 20 and 25 °N. The maximum value of warming LST difference is around 1.97 K, and the cooling magnitude is greater than the warming which reached at −4.22 K. In addition to the LST changes from 2003 to 2018, the reason for this difference may also be due to large errors caused by missing data in the south of China.

Fig. 5 shows the spatial distribution of the annual amplitude of LST in China in 2003, 2006, 2009, 2012, 2015, and 2018. Contrary to the annual mean LST, the annual amplitude of LST increases with increasing latitude: it had high values in the northern regions and low values in the southern regions. This is because with the increase in latitude, the solar elevation angle changes greatly during the year, resulting in a corresponding increase in the annual amplitude of LST. The amplitude in most regions in China increases with the increase in latitude, but there are still some regions which do not conform to this pattern. The Junggar Basin is located in the northwest part of China,

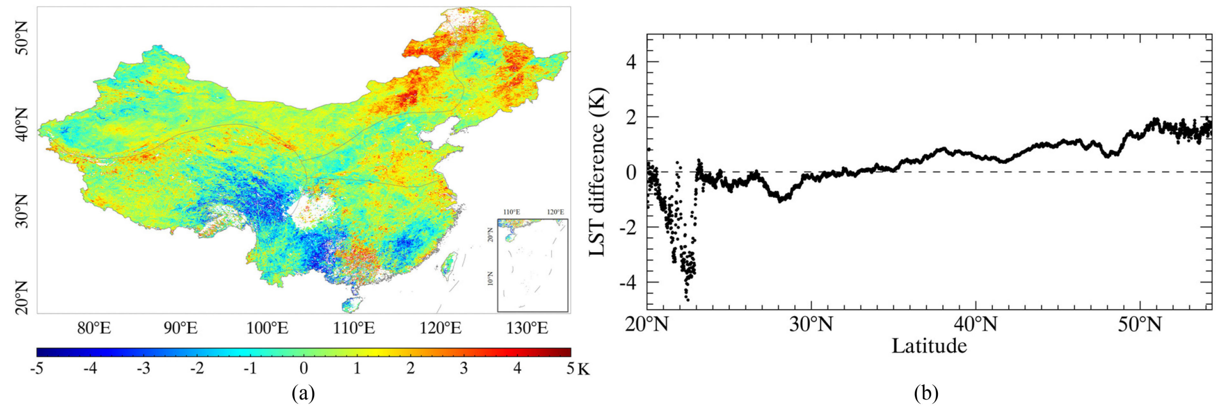

Fig. 4. (a) Spatial distribution of the annual mean LST difference between 2018 and 2003. (b) Variation of the annual mean LST difference between 2018 and 2003 in different latitude.

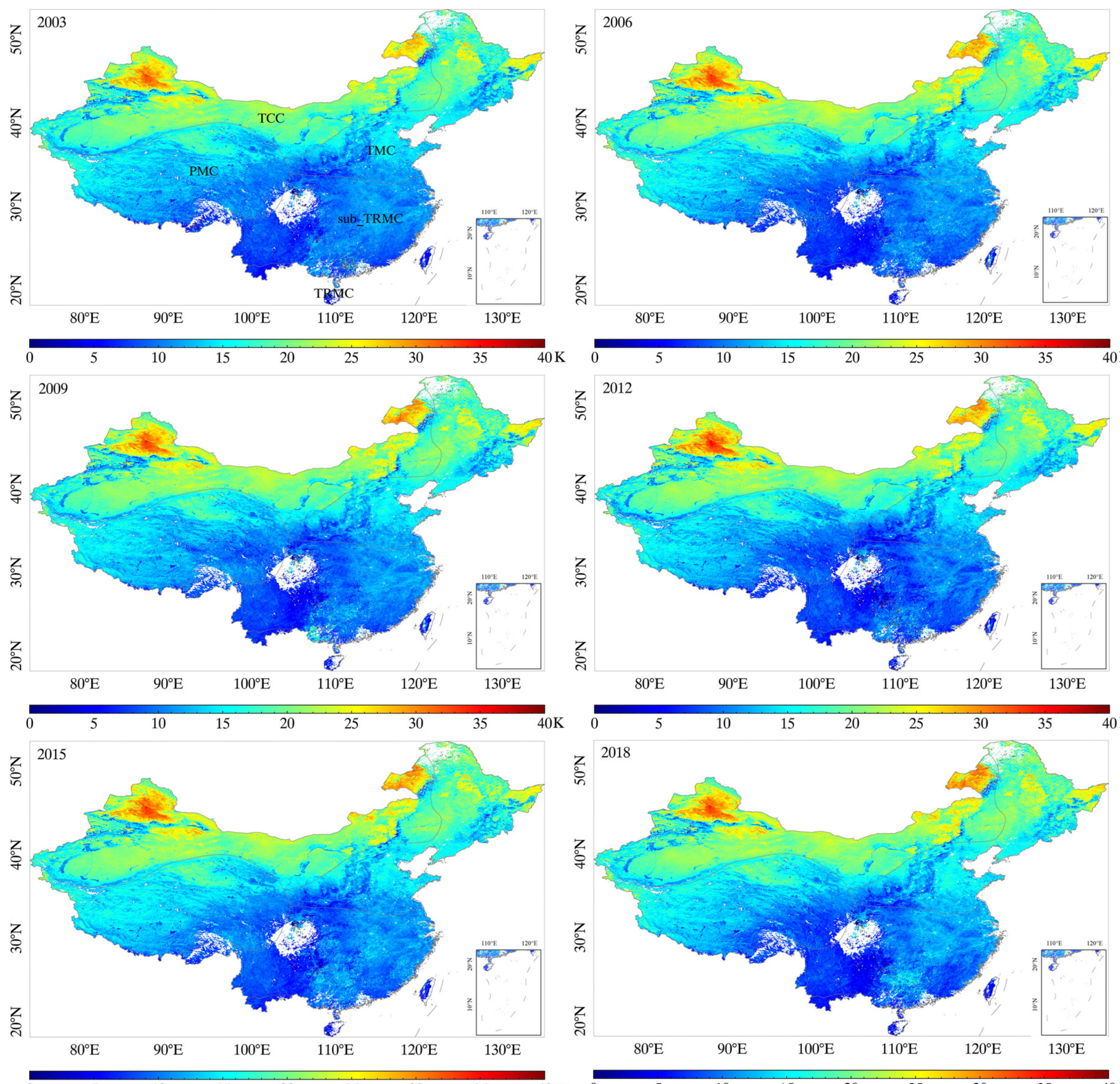

Fig. 5. Spatial distribution of the annual amplitude of LST in 2003, 2006, 2009, 2012, 2015, and 2018. The blank areas are pixels with missing data due to the impact of cloudy and rainy weather.

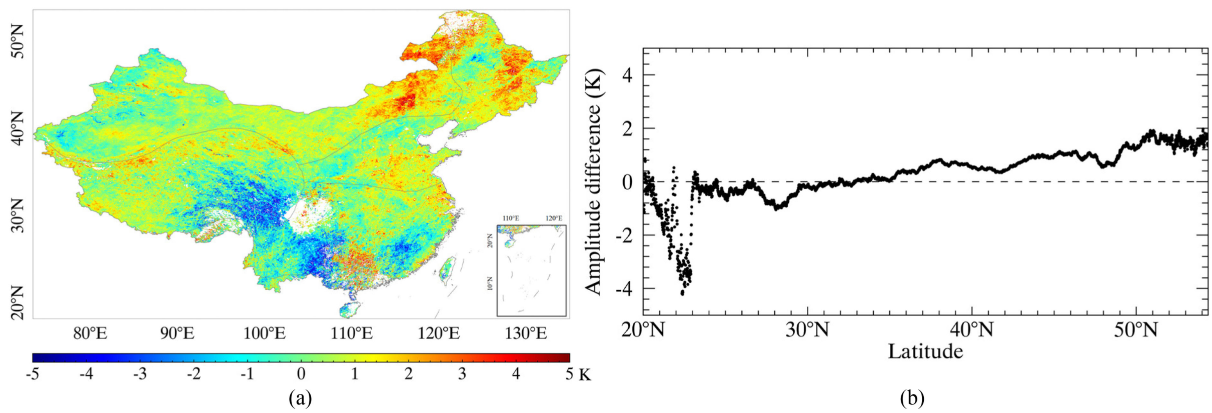

Fig. 6. (a) Spatial distribution of the annual mean amplitude difference between 2018 and 2003. (b) Variation of the annual mean amplitude difference between 2018 and 2003 in different latitude.

where the annual amplitude of LST is significantly higher than that of the northeastern part of China at the same latitude. This observation can be attributed to the factors of high latitude and below average annual rainfall. In addition, desert cover may be another reason for the increase in annual amplitude of LST because barren land is more prone to variations of LST than land covered by vegetation.

Regarding the northeast region in China, the amplitude of LST of high-altitude mountainous areas is generally smaller than that of the low-altitude plains. This is because the higher the altitude, the thinner the air. This makes the surface dissipate heat faster in summer and leads to minimal heat dissipation in winter. The Greater Khingan Range can be considered as the boundary region with regard to the annual amplitude of LST. In the west, the Khingan Range blocks the warm and humid air currents brought by the summer monsoon, resulting in a decrease in annual precipitation and an increase in the amplitude of LST. On the contrary, the eastern part faces more precipitation and shows a decrease in amplitude.

Looking at the difference in annual amplitude from each climate zone, it is observed that the TCC region has the largest amplitude, with an annual mean amplitude of more than 20 K, while the TRMC region has the smallest amplitude, with an annual mean amplitude of approximately 6 K. This is mainly due to the difference in the solar elevation angle in these regions. While TCC has the largest change in solar elevation angle, as it is located in the northern region of China, the solar elevation angle varies only minimally over the year, in the TRMC region, as it is in the lowest latitude zone. The amplitude of LST in the PMC region shows a decreasing trend from the northwest part of this region to the southeastern part. The annual amplitudes of LST in this region range from 6 to 20 K, and the mean annual amplitude of LST is approximately 13 K. This is mainly because of the influence of the southeast monsoon and the precipitation in the PMC region, which shows an increasing trend from the northwest part of this region to the southeastern part. Because the specific heat capacity of water is larger, the increase in precipitation reduces the variation range of LST, i.e., it reduces the amplitude of LST.

The change of amplitude from 2003 to 2018 was also shown by the amplitude difference of 2018 minus 2003. The spatial patterns of annual mean amplitude difference and the latitudinal difference are shown in Fig. 6(a) and (b). The distribution of amplitude difference is consistent with LST difference, which showed that the amplitude difference ranged from strong cooling in the south to moderate cooling in the middle and to the warming in the north of China.

In addition to the annual mean LST and annual amplitude of LST, we also analyzed the spatial distribution of the annual phase of LST in China. Because the interannual variations of the annual phase of LST in China are not significant, only the spatial distribution of the annual phase of LST in 2018 is shown in Fig. 7(a). The corresponding frequency histogram is also displayed in Fig. 7(b). The annual phase of LST is mainly located between the 175th day and the 205th day of each year, which corresponds to the summer months from June to July in China, and the cumulative frequency of this period of the phase accounts for more than 95%.

Due to their special geographic locations and climatic conditions, there is a phase advance or lag in some areas. The circular area in blue in Fig. 7(a) is located in the Yunnan Plateau in China. Due to the low latitude of the Yunnan Plateau and the influence of multiple circulation systems, the annual rainfall in this region is relatively high. The rainy season in this region is from May to October each year, accounting for approximately 90% of the annual rainfall. Therefore, the annual phase of LST in this region arrives before the start of the rainy season. The circular area in red in Fig. 7(a) is located in the famous Yarlung Zangbo River Grand Canyon area, in the southeast of the Qinghai–Tibet Plateau. Affected by the canyon topography and the warm and humid air currents of the Indian Ocean, this area forms the world's largest precipitation belt, which reduces the rate of LST heating in this area, causing the annual phase of LST to lag each year. In addition, the areas with more obvious phase lag are the plateau lakes in the Qinghai–Tibet Plateau. Because of the large specific heat capacity of the water bodies, the temperature rises slowly, and the phase of LST is located between the 220th day and the 240th day of each year.

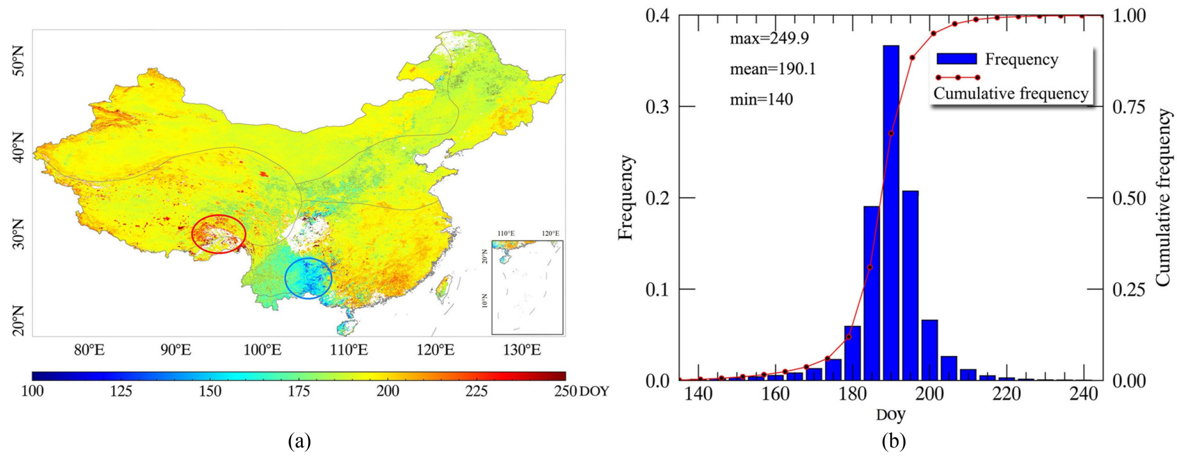

Fig. 7. (a) Spatial distribution of the annual phase of LST in 2018, along with areas with phase advance (circular area in blue) and lag (circular area in red) and (b) the corresponding frequency histogram. The blank areas are pixels with missing data due to the impact of cloudy and rainy weather.

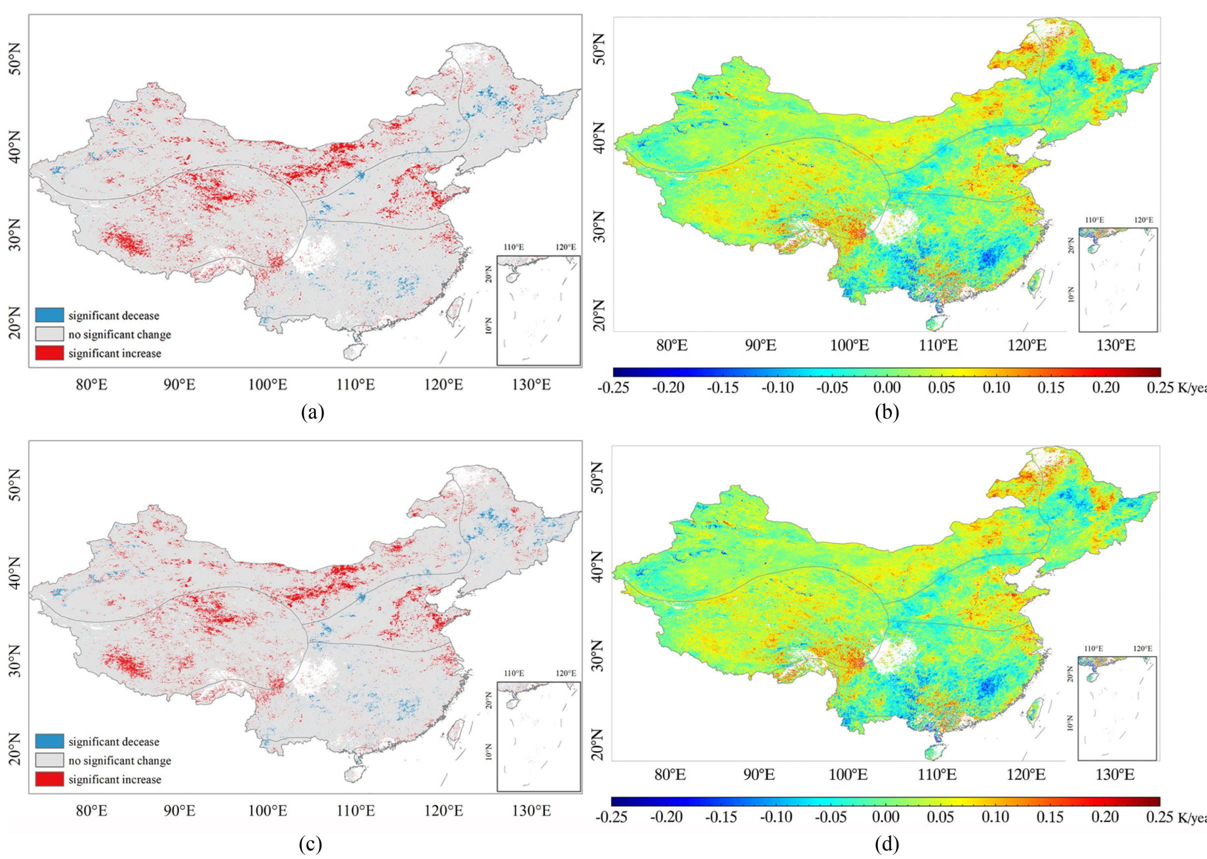

Fig. 8. Spatial distribution of the Mann–Kendall significant test of (a) annual mean LST and (b) annual amplitude of LST, and of the Theil–Sen slope of (c) annual mean LST and (d) annual amplitude of LST.

The phase change is mainly affected by long-term climate change, and shows the phenomenon of advance or lag significantly. However, given that the study period of this study is 16 years, the research results are not sufficient as a basis for climate changes. Therefore, the temporal and spatial variation characteristics of the annual phase of LST during the period were not significant.

B. Trend Analysis of Annual Mean LST and Annual Amplitude of LST

Fig. 8 shows the spatial distribution of the Mann–Kendall significance test results of the annual mean LST and annual amplitude of LST. The red, blue, and gray areas indicate the areas with a significant increase ($p < 0.05$), the areas with a

TABLE I
THEIL–SEN SLOPE STATISTICS OF ANNUAL MEAN LST AND ANNUAL AMPLITUDE OF LST IN DIFFERENT CLIMATE REGION FROM 2003 TO 2018

Climate region	Annual mean LST (K/year)*			Annual amplitude of LST (K/year)*		
	Mean	Upward proportion	Downward proportion	Mean	Upward proportion	Downward proportion
TCC	0.0546	88.42%	11.58%	0.0541	88.53%	11.48%
TMC	0.0323	59.66%	40.34%	0.0331	59.69%	40.31%
PMC	0.0848	97.93%	2.07%	0.0825	97.91%	2.09%
sub_TRMC	0.0297	53.63%	46.37%	0.0466	54.53%	45.47%
TRMC	-0.0725	26.37%	73.63%	0.0023	29.97%	70.03%
China	0.0546	79.98%	20.02%	0.0566	79.98%	20.02%

*Only statistically significant areas are counted.

significant decrease ($p < 0.05$), and the areas with no significant change in the annual mean LST and annual amplitude of LST ($p \geq 0.05$), respectively. Approximately 8.6% of the total area in China shows a significant change in the annual mean and annual amplitude. The areas with significant increase in the annual mean and annual amplitude of LST are mainly located in the TCC region, the PMC region, and the southern part of the TMC region, whereas the areas with significant decreases in the annual mean and annual amplitude are mainly located in the sub_TRMC and TRMC regions and the northern part of the TMC region.

The Theil–Sen slope results of the annual mean LST and annual amplitude of LST are also displayed in Fig. 8. The change rate of the annual mean LST and annual amplitude of LST in China varied from −0.25 to 0.25 K/year from 2003 to 2018. The rate of increase in the annual mean and annual amplitude of LST in the PMC region, the eastern area of the TCC region, and the North China Plain is greater than that in other regions. The rate of decrease in the annual mean LST and annual amplitude of LST in the southern area of the sub_ TRMC region is greater than that in the northern area of the sub_TRMC region. The variation in annual amplitude is affected by that of the annual mean LST. Therefore, the areas that show a significant change in annual amplitude are highly similar to those of the annual mean LST in the spatial distribution.

We further statistically analyzed the change trend of significant change in the annual mean LST and annual amplitude of LST in different climatic regions. The results are presented in Table I. For the annual mean LST, a significant upward trend of approximately 0.085 and 0.055 K/year is observed in the PMC and TCC regions with an upward proportion of 88.42% and 97.93%, respectively. A significant downward trend of approximately −0.073 K/year occurs in the TRMC region with a downward proportion of 73.63%. Regarding the annual amplitude of LST, the PMC and TCC regions also showed a significant upward trend of approximately 0.083 and 0.054 K/year. As a whole, the change rate of the annual mean LST and annual amplitude is approximately 0.055 and 0.057 K/year, respectively, showing an upward trend. Except for the TRMC region, the change trend of annual amplitude in other climate regions is consistent with that of the annual mean LST. The annual amplitude of LST shows a weak increasing trend in the TRMC region, while the annual mean LST shows a clearly recognizable decreasing trend. This might be because only a small proportion of LST data are available for the TRMC region.

C. Relationship Between LST and NDVI Over Different Land Cover Types

In order to further uncover the reasons for the significant changes in the annual mean LST, we also analyzed the changes in the vegetation coverage in different land cover types in areas where the annual mean LST has significantly changed (SCA, significant change area, represents the area where the LST changes significantly during the study period). In this study, the maximum value of NDVI (NDVI_max) was used to distinguish different land cover types, and the interannual change of NDVI_max was used to characterize vegetation coverage changes.

1) Interannual Variations of NDVI: The nine land cover types were obtained from grouping several land cover types according to the IGBP in the MODIS land cover product. It should be noted that the relationship between LST and vegetation coverage was analyzed within the SCA in this section. Grassland covered 29.35% of the SCA, and 23.25% of the SCA is occupied by barren land. Cropland covered 19.13% of the SCA, followed by woodland, which accounted for 15.73%. Forest occupied 7.59% of the SCA and urban areas covered 4.08%. Shrubland, wetlands, snow, and ice covered less than 1% of the SCA.

Fig. 9(a) shows the interannual variation of average NDVI_max value for each type of land cover. It can be seen that the range of NDVI_max for each type of land cover is different. NDVI_max can be utilized to clearly distinguish each type of land cover. The NDVI_max of grassland shows an obvious upward trend from 2003 to 2018, indicating that the grassland vegetation coverage increased significantly during the study period. According to the spatial distribution of grassland in Fig. 1(a), the increase of vegetation coverage in this land cover type may be related to various forage protection policies and policies of returning farmland to forests and grasslands in

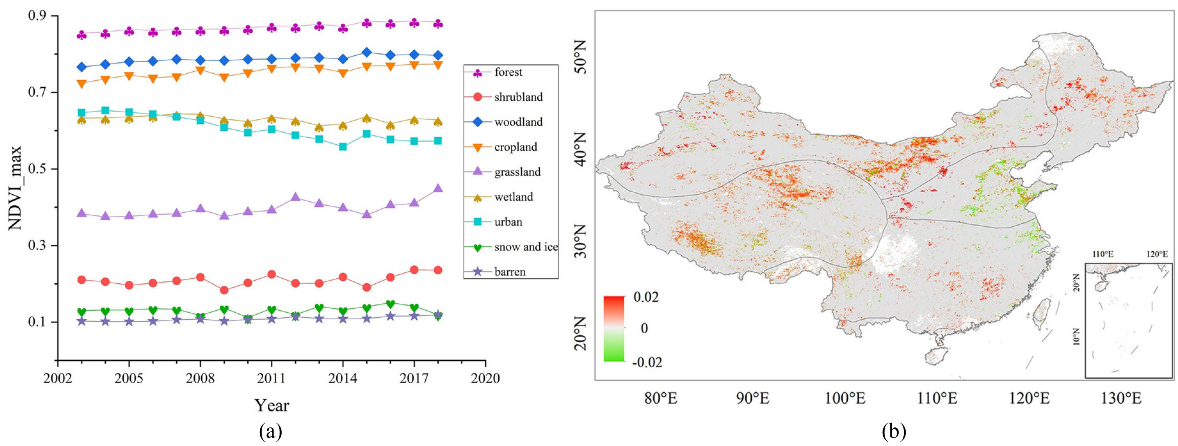

Fig. 9. (a) Interannual variations of NDVI_max over various land cover types in China. (b) Theil–Sen slope of annual NDVI_max in SCA.

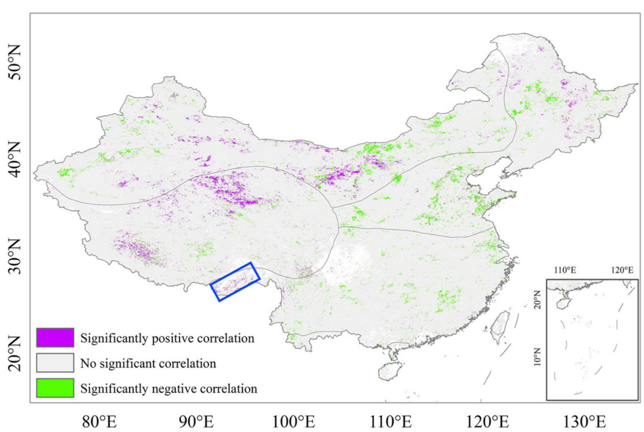

Fig. 10. Spatial distribution of the Pearson correlation coefficient between annual mean LST and NDVI_max in the SCA.

recent decades in China. The NDVI_max values of urban land and permanent wetland showed an obvious downward trend, while the other land cover types did not show any significant changes during the study period.

To further understand the vegetation dynamics during the study period, the trend analysis method was also used to obtain the trend of the annual NDVI_max in the SCA (shown in Fig. 9(b)). For the NDVI_max, more than 26.4% of the total area has a significant change. In order to correspond to the annual mean LST, Fig. 9(b) only shows the pixels in the area where the NDVI_max has a significant change in the SCA. According to Fig. 9(b), a large part of the study area has a positive effect on the vegetation growth, and the maximum increasing rate reaches 0.02 per year. The negative trend is primarily located in the south urban area of TCC region with the maximum decreasing rate of -0.02 per year.

2) Correlation Analysis Between Annual Mean LST and NDVI_max: To analyze the differences between vegetation coverage and annual mean LST among different land cover types, Pearson's correlation coefficient was used to determine NDVI_max and annual mean LST across the SCA. Fig. 10 shows the results of Pearson's correlation coefficient (r) between LST and NDVI_max. The correlation coefficient ranges from -0.98 to 0.93. The results of the significance test of the correlation coefficient show that the correlation coefficients corresponding to the regions that pass the significance test ($p < 0.05$) are mostly in the range of $r < -0.2$ or $r > 0.2$. Correlation coefficients for regions that fail the significance test range from -0.2 to 0.2. The percent area of positive correlation ($r > 0.2$) accounted for 36.5%, insignificant correlation ($-0.2 < r < 0.2$) accounted for 25.96%, and negative correlation ($r < -0.2$) accounted for 37.54%. The results show that the areas with a significant positive correlation between the annual mean LST and NDVI_max are mainly located in northwestern China and the desert areas in the Qinghai–Tibet Plateau. The forests and woodlands in the northeastern mountainous areas in China also show a positive correlation between the annual mean LST and NDVI_max. The areas with a negative correlation between the annual mean LST and NDVI_max are mainly located in the eastern grasslands of the Inner Mongolia Plateau, the cropland in the North China Plain, and the forests and woodlands in southern China.

3) Change Mechanisms in Different Land Cover Types: Fig. 11 presents the percent area of land cover types that correspond to positive and negative correlations between annual mean LST and NDVI_max. More than 55% of the areas that show a positive correlation between the annual mean LST and NDVI_max are occupied by barren land located in northwestern China and the Qinghai–Tibet Plateau. These areas have high latitudes or high altitudes, and the vegetation coverage is extremely low. Another type of land cover that shows a positive correlation between annual mean LST and NDVI_max is grassland, which accounts for 20.98% of the positively correlated pixels. Based on Fig. 1(a), it can be seen that the grassland showing a positive correlation is mainly the desert grassland in the Qinghai–Tibet Plateau. These results were largely attributed to the afforestation projects implemented by China, especially the Three North Shelterbelt Project, which has significantly increased vegetation coverage in northern China [41] and the experimental reforestation trials on the Qinghai–Tibet Plateau launched in 1999 [42]. Due to the high altitude of Qinghai–Tibet Plateau, the energy

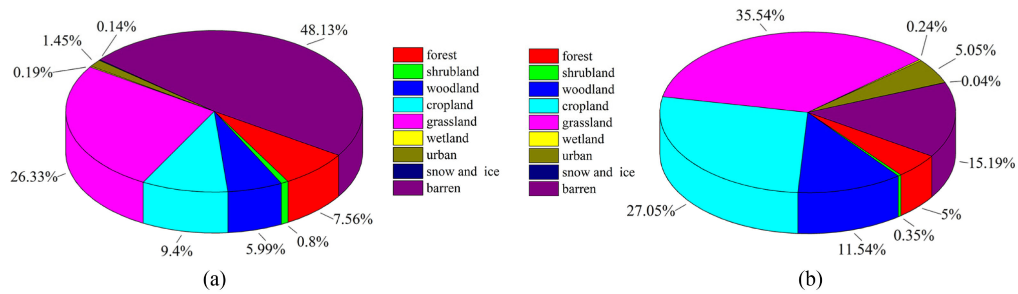

Fig. 11. Percent area of different land cover types in the correlation between NDVI_max and LST: (a) positive correlation and (b) negative correlation.

is the main limiting factor for vegetation growth, leading to a positive correlation between LST and NDVI_max. Similar conclusion was drawn in the previous study [28].

Fig. 11(b) shows a negative correlation between the annual mean LST and NDVI_max. Grassland, cropland, and woodlands accounted for a larger proportion of the negative correlation (33.94%, 31.08%, and 13.04%, respectively) between the annual mean LST and NDVI_max. The grassland areas with negative correlation are mainly located in the Inner Mongolian grasslands and plateau grasslands on the Qinghai–Tibet Plateau. Regarding Inner Mongolian grasslands, grassland degradation has always been the most serious ecological problem in this region [43]. Overgrazing has degraded pastures, resulting in an increase in exposed ground, which has increased the solar radiation absorbed by the ground and its LST. Regarding the Qinghai–Tibet Plateau, Zhong *et al*. [44] pointed out that while discerning natural and anthropogenic effects on vegetation dynamics is difficult, a significant increase in barren land was observed in this region. Huang *et al*. [45] investigated the impact of human intervention on the vegetation of the Qinghai–Tibet Plateau and reported that after 2000, the significant increase in human activities seriously affected the vitality of the vegetation in this region.

Another type of land cover with negative correlation between the annual mean LST and NDVI_max is cropland. The cropland is mainly located in the TMC area, but the annual mean LST of the cropland on the northern and southern sections of the area showed different change trends due to the temperature cooling in the northern regions and temperature warming in the southern regions. The corresponding change characteristics of NDVI_max of these portions are also different, as NDVI_max increased in the northern regions and decreased in the southern regions. While researchers have studied the correlation between the annual mean LST and NDVI_max for forests and woodlands, there is a need to discuss this topic in this study. It is an indisputable fact that China has increased its green cover since 2000s [46], [47]. In line with previous results, this study detected that the NDVI_max of forests and woodlands showed a significant upward trend during the study period. The theory that the increase in the number of trees will cool the tropical region but warm the boreal lands has been emphasized many times in previous studies [48], [49]. Nearly all forests and woodlands in China follow this theory, but there are also some special areas that show different characteristics. The area adjacent to the Yarlung Zangbo River Grand Canyon (blue rectangle in Fig. 10) belongs to the sub_TRMC zone, with the characteristics of low latitude, high temperature, and rainfall throughout the year. The annual mean LST of forests and woodlands in this area has a positive correlation with NDVI_max. Previous research shows that the terrain of this area is complex, and the climate is diverse. The study of the surface characteristics of this area should fully consider the influence of its spatial heterogeneity [50].

V. Conclusion

In this study, the spatiotemporal variability of LST in China from 2003 to 2018 was analyzed based on the MYD11A1 daily LST product. The annual mean LST, annual amplitude of LST, and annual phase of LST were derived from the continuous and derivable ATC model. The Mann–Kendall test and Theil–Sen slope were used to analyze the significant change trend of the annual mean LST and annual amplitude of LST. The influence of vegetation coverage in different land cover types on LST and the areas showing significant changes were discussed. The researchers reached the following conclusions.

1) The spatial distribution of the annual mean LST in China generally shows a pattern of high values in the southern regions and low values in the northern regions, which is in line with the law of decreasing solar radiation intensity with increasing latitude. However, elevation and land cover types also affect the spatial distribution of LST. The annual amplitude of LST shows a spatial pattern of high values in the northern regions and low values in the southern regions, which is related to the variation of the solar elevation angle.
2) The temporal variations of the annual mean LST and annual amplitude of LST were similar during the study period. In general, the LST increased in the northern regions and decreased in the southern regions, and the mean change rate of LST was 0.02 K/year. Considering different climate regions, a rapidly increasing rate of 0.03 K/year was observed in the PMC region, and the TRMC region showed a declining rate of −0.01 K/year.
3) The Mann–Kendall significance test of the annual mean LST and annual amplitude of LST shows that the areas with a significant increase in the annual mean LST and

annual amplitude of LST are mainly located in the PMC, TCC, and the southern area of the TCC regions, whereas the areas with a significant decrease in the annual mean LST and annual amplitude of LST are located in the sub_TRMC region and the northern part of the TMC region. The results of the Theil–Sen slope indicate that the change trend of the annual mean LST and annual amplitude of LST ranges from -0.01 to 0.01 K/year on a national scale, while within the SCA, the change rate of the annual mean LST and annual amplitude of LST reached 0.05 K/year.

4) There is a correlation between the annual mean LST and vegetation coverage on different land cover types. In the barren lands, the annual mean LST and vegetation coverage showed a positive correlation, while the grassland regions mainly showed a negative correlation between annual mean LST and vegetation coverage. The correlation between annual mean LST and vegetation coverage in the forest lands depended on the geographic location, as the forest land in high latitude areas showed a positive correlation between the annual mean LST and vegetation coverage, and the forest lands in low latitude areas showed a negative correlation between the annual mean LST and vegetation coverage.

References

[1] Z.-L. Li *et al.*, "Satellite-derived land surface temperature: Current status and perspectives, " *Remote Sens. Environ.*, vol. 131, pp. 14–37, Apr. 2013.

[2] F. Ji, Z. Wu, J. Huang, and E. P. Chassignet, "Evolution of land surface air temperature trend," *Nat. Clim. Change*, vol. 4, pp. 462–466, 2014.

[3] A. K. Kagawa-Viviani and T. W. Giambelluca, "Spatial patterns and trends in surface air temperatures and implied changes in atmospheric moisture across the Hawaiian islands, 1905–2017," *J. Geophys. Res.-Atmos.*, vol. 125, Jan. 2020, Art. no. e2019JD031571.

[4] J. Marotzke and P. M. Forster, "Forcing, feedback and internal variability in global temperature trends," *Nature*, vol. 517, pp. 565–570, 2015.

[5] X. Lian, Z. Zeng, Y. Yao, S. Peng, K. Wang, and S. Piao, "Spatiotemporal variations in the difference between satellite-observed daily maximum land surface temperature and station-based daily maximum near-surface air temperature," *J. Geophys. Res.-Atmos.*, vol. 122, pp. 2254–2268, Feb. 2017.

[6] S. Prakash, F. Shati, H. Norouzi, and R. Blake, "Observed differences between near-surface air and skin temperatures using satellite and ground-based data," *Theory Appl. Climatol.*, vol. 137, pp. 587–600, 2019.

[7] S. Prakash and H. Norouzi, "Land surface temperature variability across India: A remote sensing satellite perspective," *Theory Appl. Climatol.*, vol. 139, pp. 773–784, 2020.

[8] P. Fu and Q. Weng, "Temporal dynamics of land surface temperature from Landsat TIR time series images," *IEEE Geosci. Remote Sens. Lett.*, vol. 12, pp. 2175–2179, Jan. 2015.

[9] P. Fu, "Responses of vegetation productivity to temperature trends over continental United States from MODIS imagery," *IEEE J. Sel. Topics Appl. Earth Observ. Remote Sens.*, vol. 12, no. 4, pp. 1085–1090, Apr. 2019.

[10] J. Lai *et al.*, "Identification of typical diurnal patterns for clear-sky climatology of surface urban heat islands," *Remote Sens. Environ.*, vol. 217, pp. 203–220, 2018.

[11] F. Huang *et al.*, "Temporal upscaling of surface urban heat island by incorporating an annual temperature cycle model: A tale of two cities," *Remote Sens. Environ.*, vol. 186, pp. 1–12, 2016.

[12] N. Sánchez, Á. González-Zamora, J. Martínez-Fernández, M. Piles, and M. Pablos, "Integrated remote sensing approach to global agricultural drought monitoring," *Agr. Forest Meteorol.*, vol. 259, pp. 141–153, 2018.

[13] B. Bechtel, "Multitemporal Landsat data for urban heat island assessment and classification of local climate zones," in *Proc. IEEE Joint Urban Remote Sens. Event.*, 2011, pp. 129–132.

[14] B. Bechtel, "Robustness of annual cycle parameters to characterize the urban thermal landscapes," *IEEE Geosci. Remote Sens. Lett.*, vol. 9, no. 5, pp. 876–880, Sep. 2012.

[15] W. Zhao, J. He, G. Yin, F. Wen, and H. Wu, "Spatiotemporal variability in land surface temperature over the mountainous region affected by the 2008 Wenchuan earthquake from 2000 to 2017," *J. Geophys. Res.-Atmos.*, vol. 124, pp. 1975–1991, 2019.

[16] J. Quan, W. Zhan, Y. Chen, M. Wang, and J. Wang, "Time series decomposition of remotely sensed land surface temperature and investigation of trends and seasonal variations in surface urban heat islands," *J. Geophys. Res.-Atmos.*, vol. 121, pp. 2638–2657, Mar. 2016.

[17] P. Sismanidis, B. Bechtel, I. Keramitsoglou, and C. T. Kiranoudis, "Mapping the spatiotemporal dynamics of Europe's land surface temperatures," *IEEE Geosci. Remote Sens. Lett.*, vol. 15, no. 2, pp. 202–206, Feb. 2018.

[18] J. Zeng and Q. Zhang, "The trends in land surface heat fluxes over global monsoon domains and their responses to monsoon and precipitation," *Sci. Rep.*, vol. 10, 2020, Art. no. 5762.

[19] J. Aguilar-Lome, R. Espinoza-Villar, J. Espinoza, J. Rojas-Acuña, B. L. Willems, and W. Leyva-Molina, "Elevation-dependent warming of land surface temperatures in the Andes assessed using MODIS LST time series (2000–2017)," *Int. J. Appl. Earth Observ. Geoinf.*, vol. 77, pp. 119–128, 2019.

[20] E. J. Good, D. J. Ghent, C. E. Bulgin, and J. J. Remedios, "A spatiotemporal analysis of the relationship between near-surface air temperature and satellite land surface temperatures using 17 years of data from the ATSR series," *J. Geophys. Res.-Atmos.*, vol. 122, pp. 9185–9210, 2017.

[21] R. Amiri, Q. Weng, A. Alimohammadi, and S. K. Alavipanah, "Spatial–temporal dynamics of land surface temperature in relation to fractional vegetation cover and land use/cover in the Tabriz urban area, Iran," *Remote Sens. Environ.*, vol. 113, pp. 2606–2617, 2009.

[22] S. Piao, A. Mohammat, J. Fang, Q. Cai, and J. Feng, "NDVI-based increase in growth of temperate grasslands and its responses to climate changes in China," *Glob. Environ. Change*, vol. 16, pp. 340–348, 2006.

[23] Y. Julien, J. A. Sobrino, and W. Verhoef, "Changes in land surface temperatures and NDVI values over Europe between 1982 and 1999," *Remote Sens. Environ.*, vol. 103, pp. 43–55, 2006.

[24] P. Kumar, A. Husain, R. B. Singh, and M. Kumar, "Impact of land cover change on land surface temperature: A case study of Spiti Valley," *J. Mt. Sci.*, vol. 15, pp. 1658–1670, 2018.

[25] W. Nega, B. T. Hailu, and A. Fetene, "An assessment of the vegetation cover change impact on rainfall and land surface temperature using remote sensing in a subtropical climate, Ethiopia," *Remote Sens. Appl., Soc. Environ.*, vol. 16, 2019, Art. no. 100266.

[26] Y. Deng *et al.*, "Relationship among land surface temperature and LUCC, NDVI in typical Karst area," *Sci. Rep.*, vol. 8, 2018, Art. no. 641.

[27] S. S. Peng *et al.*, "Afforestation in China cools local land surface temperature," *Proc. Natl. Acad. Sci.*, vol. 111, pp. 2915–2919, 2014.

[28] A. Karnieli *et al.*, "Use of NDVI and land surface temperature for drought assessment: Merits and limitations," *J. Clim.*, vol. 23, pp. 618–633, 2010.

[29] F. Marzban, S. Sodoudi, and R. Preusker, "The influence of land-cover type on the relationship between NDVI-LST and LST-Tair," *Int. J. Remote Sens.*, vol. 39, pp. 1377–1398, 2018.

[30] Z. Xing *et al.*, "Modeling year-to-year variations of clear-sky land surface temperature using Aqua/MODIS data," *IEEE Access*, vol. 8, pp. 114541–114553, 2020.

[31] S. Williamson, D. Hik, J. Gamon, J. Kavanaugh, and G. Flowers, "Estimating temperature fields from MODIS land surface temperature and air temperature observations in a sub-Arctic alpine environment," *Remote Sens.*, vol. 6, pp. 946–963, 2014.

[32] S. Duan, Z. Li, H. Wu, B. Tang, X. Jiang, and G. Zhou, "Modeling of day-to-day temporal progression of clear-sky land surface temperature," *IEEE Geosci. Remote Sens. Lett.*, vol. 10, no. 5, pp. 1050–1054, Sep. 2013.

[33] S. Prakash and H. Norouzi, "Land surface temperature variability across India: A remote sensing satellite perspective," *Theory Appl. Climatol.*, vol. 139, pp. 773–784, 2020.

[34] B. Bechtel, "A new global climatology of annual land surface temperature," *Remote Sens.*, vol. 7, pp. 2850–2870, 2015.

[35] B. Bechtel and P. Sismanidis, "Time series analysis of moderate resolution land surface temperatures," in *Remote Sensing Time Series Image Processing*. Q. Weng, Ed. Boca Raton, FL, USA: CRC Press, 2018, pp. 111–142.

[36] H. B. Mann, "Nonparametric tests against trend," *Econometrica*, vol. 13, no. 3, pp. 245–259, 1945.

[37] P. K. Sen, "Estimates of the regression coefficient based on Kendall's tau," *J. Amer. Stat. Assoc.*, vol. 63, pp. 1379–1389, 1968.

[38] M. Gocic and S. Trajkovic, “Analysis of changes in meteorological variables using Mann-Kendall and Sen’s slope estimator statistical tests in Serbia,” *Glob. Planet. Change*, vol. 100, pp. 172–182, 2013.
[39] Y. Xu, Y. Shen, and Z. Wu, “Spatial and temporal variations of land surface temperature over the Tibetan plateau based on harmonic analysis,” *Mt. Res. Dev.*, vol. 33, pp. 85–94, 2013.
[40] T. Phan, M. Kappas, and T. Tran, “Land surface temperature variation due to changes in elevation in northwest Vietnam,” *Climate*, vol. 6, p. 28, 2018, Art. no. cli6020028.
[41] Y. Zhang, Y. Yao, X. Wang, Y. Liu, and S. Piao, “Mapping spatial distribution of forest age in China,” *Earth Space Sci.*, vol. 4, pp. 108–116, 2017.
[42] G. Miehe *et al.*, “An inventory of forest relicts in the pastures of southern Tibet (Xizang A.R., China),” *Plant Ecol.*, vol. 194, pp. 157–177, 2007.
[43] X. Zhang *et al.*, “Understanding grassland degradation and restoration from the perspective of ecosystem services: A case study of the Xilin river basin in inner Mongolia China,” *Sustainability*, vol. 8, p. 594, 2016, Art. no. su8070594.
[44] L. Zhong, Y. Ma, Y. Xue, and S. Piao, “Climate change trends and impacts on vegetation greening over the Tibetan plateau,” *J. Geophys. Res.-Atmos.*, vol. 124, pp. 7540–7552, 2019.
[45] K. Huang, Y. Zhang, J. Zhu, Y. Liu, J. Zu, and J. Zhang, “The influences of climate change and human activities on vegetation dynamics in the Qinghai-Tibet plateau,” *Remote Sens.*, vol. 8, p. 876, 2016, Art. no. ijerph13010019.
[46] S. Piao *et al.*, “Characteristics, drivers and feedbacks of global greening,” *Nat. Rev. Earth Environ.*, vol. 1, pp. 14–27, Jan. 2020.
[47] Z. Zhu *et al.*, “Greening of the earth and its drivers,” *Nat. Clim. Chang.*, vol. 6, pp. 791–795, 2016.
[48] X. Lee *et al.*, “Observed increase in local cooling effect of deforestation at higher latitudes,” *Nature*, vol. 479, pp. 384–387, 2011.
[49] G. B. Bonan, “Forests and climate change: Forcings, feedbacks, and the climate benefits of forests,” *Science*, vol. 320, pp. 1444–1449, 2008.
[50] J. Li *et al.*, “Longer conserved alpine forests ecosystem exhibits higher stability to climate change on the Tibetan plateau,” *J. Plant Ecol.*, vol. 12, pp. 645–652, 2019.

Yanru Yu received the B.S. degree in management and the M.S. degree in geological engineering from Hebei GEO University, Hebei, China, in 2014 and 2018, respectively. She is currently pursuing the Ph.D. degree in agricultural remote sensing from the Institute of Agricultural Resources and Regional Planning, Chinese Academy of Agricultural Sciences, Beijing, China, in 2018.

Her research interest includes agricultural quantitative remote sensing.

Si-Bo Duan received the Ph.D. degree in cartography and geographical information system from the Institute of Geographic Sciences and Natural Resources Research, Chinese Academy of Sciences, Beijing, China, in 2014.

He is currently an Associate Professor with the Institute of Agricultural Resources and Regional Planning, Chinese Academy of Agricultural Sciences, Beijing, China. His current research interests include the retrieval and validation of land surface temperature.

Zhao-Liang Li received the Ph.D. degree in geophysics and remote sensing from the University of Strasbourg, Strasbourg, France, in 1990.

Since 1992, he has been a Research Scientist with CNRS, Illkirch, France. He joined the Institute of Agricultural Resources and Regional Planning, Beijing, China, in 2013. He has participated in many national and international projects, such as NASA-funded MODIS, EC-funded program EAGLE, and ESA-funded programs SPECTRA. His research interests include thermal infrared radiometry, parameterization of land surface processes at large scale, as well as in the assimilation of satellite data to land surface models.

Sheng Chang received the Ph.D. degree in remote sensing of resources and environment from the Central South University, Changsha, China, in 2018.

He joined the Aerospace Information Research Institute, Chinese Academy of Sciences, Beijing, China, in 2009. He has participated in many national and international cooperation projects, such as International Cooperation Project of the National Key R & D Program (China–U.K., China–European), UNESCAP, CAS-TWAS, the National Natural Science Foundation, the National Science and Technology Support Program, etc. His research interests include surface parameters inversion at multiscale, agricultural and water resource remote sensing, as well as in the monitoring and prediction of agricultural disasters.

Zefeng Xing received the B.E. degree in remote sensing of technology from the Heilongjiang Institute of Technology, Heilongjiang, China, in 2013, the M.S. degree in cartography and geographic information system from the University of Chinese Academy of Sciences, Beijing, China, in 2016, and the Ph.D. degree in agricultural remote sensing from the Chinese Academy of Agricultural Sciences, Beijing, China, in 2020.

He is currently a Postdoc with the Ministry of Agriculture, Chinese Academy of Agricultural Engineering, Beijing, China.

Pei Leng received the Ph.D. degree in geographic information system from the University of Chinese Academy of Sciences, Beijing, China, in 2015.

He is currently with the Key Laboratory of Agricultural Remote Sensing, Ministry of Agriculture/Institute of Agricultural Resources and Regional Planning, Chinese Academy of Agricultural Sciences, Beijing, China. His research interests include the moisture and energy fluxes from remote sensing data.

Maofang Gao was born in Shandong, China. She received the bachelor’s degree in geography from Northeast Normal University, Jilin, China, in 2003, the master’s degree in cartography and geography information system from Nanjing University, Jiangsu, China, in 2006, and the Ph.D. degree in agricultural remote sensing from the Chinese Academy of Agricultural Sciences, Beijing, China, in 2011.

Since 2006, she has been a Research Staff with the Institute of Agricultural Resources and Regional Planning, Chinese Academy of Agricultural Sciences. Since 2015, she has been an Associate Professor. Her research interests include quantitative remote sensing and agricultural drought monitoring.